Current Applied Physics 45 (2023) 64–71

Contents lists available at ScienceDirect

Current Applied Physics

journal homepage: www.elsevier.com/locate/cap

Molecular dynamics analysis of water flow through a multiply connected carbon nanotube channel

Ermioni Papadopoulou [a], Gwan Woo Kim [b], Petros Koumoutsakos [a,c], Gunn Kim [b,*]

[a] Computational Science and Engineering Laboratory, ETH Zürich, Zürich, CH-8092, Switzerland
[b] Department of Physics and HMC, Sejong University, Seoul, 05006, Republic of Korea
[c] Gordon McKay Professor of Computing in Science and Engineering, Pierce Hall, 29 Oxford Street, Cambridge, 02138, MA, USA

ARTICLE INFO

Keywords:
Multiply connected carbon nanotube
Nanofluidics
Imbibition
Water transport
Molecular dynamics

ABSTRACT

The filling process of nanoconduits is an active research topic. In this study, we use molecular dynamics simulations to identify the filling process of water molecules in a multiply connected carbon nanotube (MCCNT). For water permeation, a local change in the channel cross-section affects the water filling of MCCNTs because it may lead to irregularities in the permeation profile. A decrease in hydrogen bonds at the junctions of the structure characterizes the permeability of MCCNTs. In contrast to pristine CNTs, the complex nanochannel exhibits a different imbibition profile due to the energy changes at the junction. Next, we examine the local water density and velocity patterns in MCCNT channels to understand how junction regions affect steady-state water transport. We find that there is congestion and irregularities in steady water flow density and velocity profiles. Through this study, we expect to develop effective channels with more complex geometries for water purification and drug delivery.

1. Introduction

Nanotechnology is one of the most promising technologies for water purification and desalination [1]. Particularly, carbon nanotube (CNT) membranes have attracted much attention due to their unique osmotic properties [2], enhanced water permeability [3–6], and high ion selectivity [7]. There is a concern with CNT-based filtration systems due to an enormous pressure difference that must be applied through the tube to drive the water transport [6]. Using Y-junctions of nanotubes of varying sizes may alleviate the pressure required for the filling process and enhance the membrane's filtration. It has become increasingly interesting to study water flow through dendritic formations of CNTs [8], where one CNT part splits into two smaller tubes at a Y-junction [9,10].

The confinement of water inside a CNT is an exciting research topic in experiment and theory. Water transport through a single CNT has been extensively studied using molecular dynamics (MD) simulations [11–15,6]. On the other hand, density functional theory calculations predict the adsorption properties of a single water molecule or an ice-like structure in cylindrical CNTs [16–20]. The water flow through junctions of CNTs or combinations of CNTs with graphene sheets has been of great scientific interest because the sizes of the junctions may alter fluid dynamics phenomena locally [21,22].

However, previous research has focused on simple cylindrical CNT structures. MD studies have shown that a converging junction can accelerate the flow [23], while flows in converging and then diverging junctions are faster than those in the opposite direction [24]. The nonequilibrium imbibition phenomena at the nanojunction depend on the size of each region of the junction [24]. To date, computational simulations of CNT Y-junctions have concentrated on static ice-like structures or macroscopic observables such as flux and pressure losses [25–28].

Unlike cylindrical CNTs, multiply connected carbon nanotubes (MCCNTs) have complex topological structures, so their cross-sectional area is not uniform. The nanostructures can be formed by CNTs of various sizes that stick to each other under the influence of an electron beam to form Y-junctions [29–32]. Experimental evidence of Y-junctions of CNTs revealed a "zipper" mechanism at the nanoscale during the coalescence of two single-wall CNTs [33,34]. The coalescence of CNTs through Y-junctions has been found to exhibit intriguing electronic properties [35,36], and the CNTs have been considered building blocks for all-carbon nanowires [37]. Such CNTs may also be considered possible components of desalination and water purification devices.

* Corresponding author.
E-mail address: gunnkim@sejong.ac.kr (G. Kim).

https://doi.org/10.1016/j.cap.2022.11.003
Received 13 September 2022; Received in revised form 1 November 2022; Accepted 3 November 2022
Available online 12 November 2022

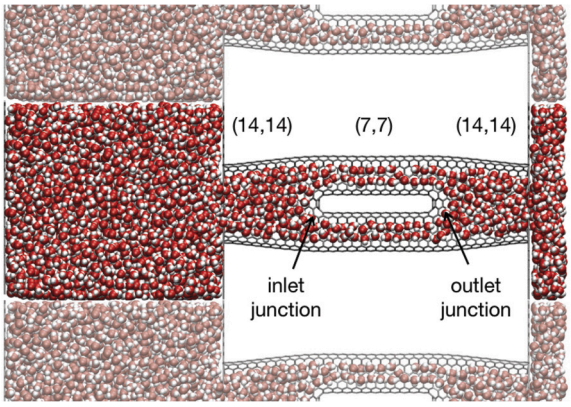

Fig. 1. Model structure of the MCCNT connected to two reservoirs after water filling in the tube channel. The model is displayed in the x- and z-directions. The periodic images of the system in the x-direction are displayed in reduced opacity.

In this study, we investigate water flowing through an MCCNT structure (Fig. 1). We focus on the flow dynamics through the MCCNT, following a previous study investigating equilibrium structures of water molecules in the MCCNT [38]. To the best of our knowledge, only a few studies have concentrated on pressure-driven water transport in CNT structures with locally varying cross-sectional areas [24] or on the characterization of the nanochannel filling process [39–41]. In particular, we quantify how the Y-junctions of the MCCNT induce features like "traffic congestion." If water is modeled as a continuum, it is difficult to explain this congestion feature. Rather than continuous fluid models, we use MD simulations to understand fluid transport phenomena in nanostructures with locally varying cross-sectional areas since the width and length of nanochannels in MCCNTs are comparable to the distance between H_2O molecules.

2. Computational methods and models

We study water transport characteristics in an MCCNT channel connecting two reservoirs. As shown in Fig. 1, each (14, 14) CNT has two arms of (7, 7) tubes in between. The total length of the MCCNT structure is ~ 8 nm. In the MCCNT, the length of each (14, 14) CNT is approximately 2.4 nm, and the length of each (7, 7) CNT arm is about 3.2 nm. For comparison, we also simulate water transport through plain (7, 7) and (14, 14) CNTs. Both ends of the CNTs are bonded to the graphene sheets at the reservoirs [42]. In the MCCNT, the (14, 14) CNTs have elliptical cross-sections because they are joined at each junction with the (7, 7) CNT arms. In Supplementary Information (SI), Section 1.1 provides further details on the MCCNT structure. Periodicboundary conditions are applied in the supercell's lateral directions (x and y), with a box length equal to the period of graphene sheets in both directions (~ 5 nm). There is no periodicity in the tube's axial (z) direction. The supercell boundary in the z-direction is placed 6 nm away from the outlet graphene sheet to allow water to accumulate at the outlet reservoir.

We divide the simulation process of all nanotube structures into two stages: the nonequilibrium filling and the steady-state transport of water. For the filling process of each nanotube [MCCNT, (7, 7) and (14, 14) CNTs], the tube is connected to two reservoirs. Initially, one reservoir is filled with 4085 water molecules. The system is first equilibrated in the reservoir at constant pressure and constant temperature (NPT) ensemble for 5 ns, keeping temperature and pressure constant at 298 K (25 °C) and 1 bar (≈ 1 atm), respectively, with a Nosé–Hoover thermostat and a Parrinello-Rahman barostat [43,44] with damping constants of 100 and 1000 time steps, respectively. After equilibration, one end of the reservoir containing water is connected to an empty MCCNT. Then, a piston-like force of 3.12, 6.25, or 12.5 pN per atom is applied to the outer graphene sheet of the reservoir, which induces water through the nanochannel, causing a pressure difference of 125, 250, or 500 MPa, respectively, between the inlet and outlet of the MCCNT. Such pressure drop values were selected to match the lower limits for pressure-driven flow [6,45]. The barostat is turned off during production runs when the piston force is used to pressurize the nanochannel. The filling process is completed when the water density profile of the nanochannel does not change over time. The local density of water is measured in the (7, 7) and (14, 14) CNT regions of the MCCNT. By repeating the simulation five times at 298 K, the initial velocity distribution of the water molecules is modified to obtain a statistical average of the quantity of interest.

After the filling process, we simulate constant water flow through the channel for 5 ns, applying the same force to the outermost graphene sheet of the left water reservoir, which corresponds to a pressure difference between the inlet and outlet of the MCCNT equal to 500 MPa. The initial configuration of the steady-state transport simulation is different for each nanotube. The two reservoirs connected to the nanotubes are initially filled with water, one with 4085 water molecules and the other with 505 water molecules. The water in the reservoir is previously equilibrated with a Nosé–Hoover thermostat and a Parrinello-Rahman barostat at a pressure of 298 K and 1 bar in the NPT ensemble [43,44] with damping constants of 100 and 1000 time steps, respectively. The equilibrated water in the complex nanotube structure is extracted from a filling simulation at a pressure of 500 MPa and used as an initial configuration for a steady-state transport simulation. The model systems contain 330 water molecules in the MCCNT, 540 in the (14, 14) CNTs, and 70 in the (7, 7) CNTs, respectively. In all production simulations, the water molecules are maintained at a temperature of 298 K, adjusting only the thermal component of temperature, which was found to be equivalent to a non-thermostatted system (see SI, Section 1.3).

All MD simulations are performed with the LAMMPS package [46]. We apply a time step of 1 fs and periodic boundary conditions. With molecular topology constraints imposed by the SHAKE algorithm [47], TIP4P-Ew water-molecule interactions [48,49] are used. For short-range interactions, we use a cutoff of 1.0 nm for the O-O pair [50]. For long-range electrostatic interactions, we use a particle-particle particle-mesh (P3M) algorithm [51] with a cutoff distance of 0.85 nm [48] and a root-mean-squared error in the force calculation of 10^{-5}. In all simulations, the Dreiding potential [52] describes the interactions of the carbon atoms. A Lennard-Jones potential describes the nonbonding interactions between an oxygen atom in a water molecule and carbon atoms of graphene or the CNT with a cutoff of 1.2 nm for the C-O pair [52]. The potential produces a slightly hydrophobic water contact angle of 110° for the interaction of water with carbon atoms of the CNT [53]. A neutral water contact angle of ≈90° for the interaction of water with carbon atoms of the graphene sheet [12,54]. Visualizations are performed with the Visual Molecular Dynamics (VMD) package [55].

We build the graphene sheets and the CNTs with the WCCNT package developed within the CSELab [56]. The package works within the VMD software interface [55] as a TCL plugin, and it integrates different routines to generate and analyze LAMMPS-compatible files of graphene sheets (GRSs) and carbon nanotubes (CNTs) with water. We also use TCL scripting within the VMD package for preparing the systems, including creating missing bonds between graphene sheets and carbon nanotubes.

3. Results and discussion

When it comes to transport characteristics of water molecules through the MCCNT, we distinguish between nonequilibrium water filling and steady-state water transport. Water density and velocity profiles in the MCCNT are compared to those in the pristine (7, 7) and (14, 14) CNTs, which correspond to the narrower and wider tubes of the MCCNT, respectively.

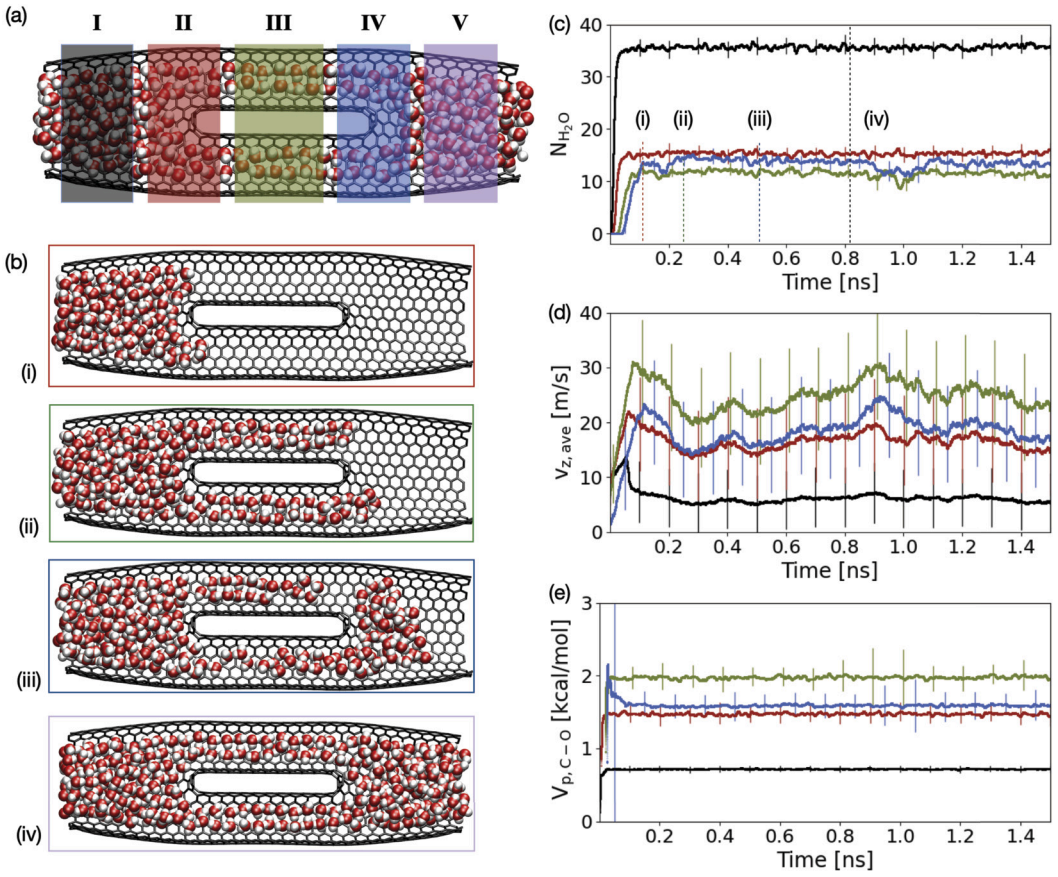

Fig. 2. The nonequilibrium process of water filling the MCCNT. (a) The MCCNT is split into 5 zones, denoted with colors and Latin numbering. (b) The instances of the flow in the MCCNT when water fills each local colored zone of (a). The colors of the frames of the subfigures correspond to the color of each local zone in (a); (b-i), (b-ii), (b-iii), and (b-iv) correspond to the instances where the local zones II, III, IV, and V are filled with water, respectively. (c) Time series measurements of the number of water molecules, N_{H_2O}, recorded at specified zones along the length of the MCCNT. (d) Average local velocity, v_z, ave. (e) Interaction energy between carbon and water molecules, $V_{p,C-O}$. The time series of each measured variable is colored according to the corresponding local zone of measurement: black, red, green, and blue curves correspond to the measurements recorded in the I, II, III, and IV zones of the MCCNT in (a). We omit the representation of the water reservoirs in (a). The graph lines in (c-e) represent the statistical average of five simulation samples for pressure force corresponding to $\Delta p = 250$ MPa. The error bars represent the standard deviation over the samples. (For interpretation of the colors in the figure(s), the reader is referred to the web version of this article.)

3.1. Nonequilibrium water filling in MCCNT

In the first step, we compare the MCCNT, the pristine (14, 14) CNT, and the pristine (7, 7) CNT to study the nonequilibrium process of filling empty nanotubes with water. Each model structure has a length that is approximately the same. Three pressure drops are considered for each channel: 125, 250, and 500 MPa between the inlet and outlet reservoirs. We use the statistical mean of the trajectories from five simulation results for each tube and pressure in the analysis. Each sample is given a random initial velocity distribution of the Gaussian type.

To analyze the filling process, we identify five regions along the MCCNT: (I) the left (14, 14) CNT region; (II) the left (inlet) Y-junction; (III) the (7, 7) CNT arms; (IV) the right (outlet) Y-junction; and (V) the right (14, 14) CNT region, as shown in Fig. 2a. In turn, Fig. 2b shows the snapshots of filling stages (i) – (iv) of the last four regions (II – V) obtained from the MD simulations. From simulation post-processing, we obtain the time taken to complete the filling of the MCCNT channel and the relative time percentage needed to fill each of its regions, defining, therefore, the filling stages of the MCCNT (Table 1). We consider each region filled with water when the number of water molecules occupying the region reaches a terminal value.

In Table 1, we compare the filling of the MCCNT with the cases of the pristine (14, 14) and (7, 7) CNTs. The first two rows of the table represent the pristine CNTs. Time measurements are normalized with the time taken to complete the water filling of the pure (14, 14) CNT. In

Table 1
Comparison of the filling of three nanochannels: the MCCNT, the pristine (14, 14) CNT, and the pristine (7, 7) CNT. We compare the time evolution of the channels' filling process, i.e., the time taken for each filling stage of the channels, for the pressure difference applied between the two reservoirs connected by the nanotubes. The resulting values are averages over 5 statistical samples, with the standard deviation of filling times kept below 9% for all pores and pressures. All results are presented in arbitrary units (a.u.) as time measurements are normalized according to the time taken for the pristine (14, 14) CNT to be filled. The empty rows of the table indicate non-filling conditions of the respective region/nanotube for the specified Δp. The labels of the MCCNT zones correspond to the colored zones of Fig. 2a.

Δp [MPa]	cumulative time [a.u.]		
	125	250	500
(14, 14) CNT	1.00	1.00	1.00
(7, 7) CNT	-	3.24	2.56
MCCNT (region I)	0.23	0.27	0.43
region II	0.61	0.55	0.59
region III	1.18	1.11	1.13
region IV	-	2.34	2.13
region V	-	2.79	2.44

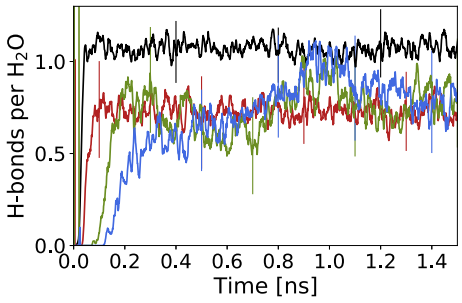

Fig. 3. Time evolution of the number of hydrogen bonds per water molecule formed during the nonequilibrium filling of the MCCNT with water. The colors of the four different curves correspond to the local zone of measurement: black, red, green, and blue curves correspond to the measurements recorded in the I, II, III, and IV zones of the MCCNT in Fig. 2(a). Over five simulation samples, the error bars represent the standard deviation, and the lines represent the statistical average.

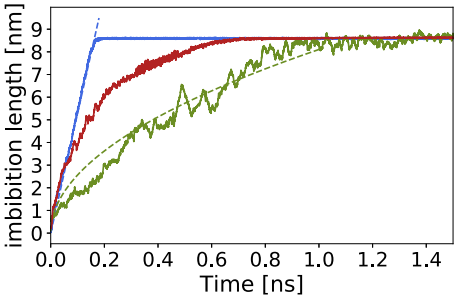

Fig. 4. Time evolution of the imbibition length for the MCCNT (red curve), the (14, 14) CNT (blue curve), and the (7, 7) CNT (green curve) for a pressure force corresponding to a $\Delta p = 250$ MPa.

other words, every value in Table 1 corresponds to the ratio of absolute time to fill the region to the time it takes to fill the (14, 14) CNT with water. Blank rows indicate the unfilled states of the area. For instance, when the pressure is 125 MPa, water molecules do not practically enter the (7, 7) CNT arm. The next four rows show the filling time of the MCCNT as local measurements through the MCCNT. Each row corresponds to a region along the axis of the MCCNT, as shown in Fig. 2a. Interestingly, water does not fill the MCCNT at 125 MPa. Water molecules enter the (7, 7) CNT arm but not the (14, 14) CNT region on the right. At a pressure of 125 MPa, neither the pristine (7, 7) CNT nor the MCCNT is entirely filled with water from end to end, indicating how high the pressure must be applied to the nanotubes for imbibition. The filling of the (7, 7) CNT with water takes 3.24 times (2.56 times) longer than that of the (14, 14) CNT at 250 MPa (500 MPa). The MCCNT only fills the region III (or the (7, 7) CNT arm) during the time that corresponds to filling the (14, 14) tube. Interestingly, also at pressures of 250 and 500 MPa, the time to completely fill CNTs with water is nearly the same as that of region III of the MCCNTs. We explain the imbibition later in the text in more detail.

We count the number of water molecules N_{H_2O} to determine the local water density as a function of time for each zone (from zone I to V). To better understand the interaction between water molecules and the tube wall, we compute the interaction energy $V_{p,C-O}$ between the O atom in a H_2O molecule and the C atom in the CNT. We also compute the local average velocity $v_{z,ave}$, in four different regions. The regions along the MCCNT axis are denoted by different colors in Fig. 2a. For example, the filling time of region II in Fig. 2c corresponds to the time instance shown in Fig. 2(b-i). Fig. 2(c) shows the number of water molecules in each zone. In Fig. 2(d), the average axial velocity of the water molecules is presented. Fig. 2(e) shows the interaction energy between carbon atoms at the tube wall and oxygen atoms in the water molecules at the interface for a pressure force corresponding to $\Delta p = 250$ MPa. We further calculate the number of hydrogen bonds through the filling trajectory of the MCCNT in the predefined four regions for the same Δp (Fig. 3).

Compared to the (7, 7) CNT, the (14, 14) CNT has twice the diameter and thus have four times the cross-sectional area. Since the MCCNT has two (7, 7) CNT arms, the number of water molecules in zone I is almost double that in zone III. The number of hydrogen bonds in each zone has a similar pattern (Fig. 3). H_2O molecules rapidly enter the left (14, 14) CNT part until $t \approx 1$ ns and $v_{z,ave}$ approaches 16 m/s at ~ 1 ns ((Fig. 2d)). Interestingly, the velocity $v_{z,ave}$ suddenly decreases to less than 10 m/s after water molecules fill zone II at around 1 ns. This trend continues with small variations around an average value.

The number of hydrogen bonds decreases when water molecules enter the empty (7, 7) CNT arms. This phenomenon occurs due to the confinement of water molecules in a two-row channel in the (7, 7) CNT. H_2O molecules form strong hydrogen-bond networks in 3D bulk water. In contrast, when confined in a CNT, water molecules at the interface have van der Waals interactions with the CNT wall, which are weaker than hydrogen bonds. From the perspective of water molecules at the interface, the number of adjacent water molecules decreases and the interaction with the nanotube walls is weak, resulting in energy loss. In other words, since the ratio of the surface area to the volume of the water column or water chain contained in the CNT with a small radius is large, energy loss occurs due to the decrease in hydrogen bonds. Therefore, a smaller radius-CNT is not favorable for water imbibition.

Therefore, in the MCCNT setting, water molecules do not effortlessly enter the (7, 7) tubes. Once inside the (7, 7) CNT arms, water molecules speed through, as shown in Fig. 2(d), towards the outlet junction. At the outlet junction, it is energetically beneficial for water molecules to rapidly exit towards the outlet (14, 14) CNT arm and form hydrogen bonds with the neighboring molecules. By rapidly leaving the (7, 7) arm, water molecules can break the hydrogen bonds at the outlet junction. An event of hydrogen bond breakage within the (7, 7) CNT arm is seen in Fig. 2(b-iii). The green curve in Fig. 2c highlights this, with N_{H_2O} reaching a minimum around $t = 0.6$ ns, and the hydrogen bonding network in Fig. 3 weakening around $t = 0.6$ ns. The hydrogen bond breakage within the (7, 7) CNT arms leads to the local increase of the interaction energy between carbon and water molecules in comparison to the pair energy per water molecule in the (14, 14) CNT, as shown in Fig. 2e. The (7, 7) CNT arms are filled with H_2O molecules in about 0.4 ns for each snapshot of Figs. 2(b-i) and (b-ii). Another exciting point is that the blue curve, which represents the nature of the water in region IV, increases gradually until equilibrium values are obtained, both from the perspective of N_{H_2O} and $V_{p,C-O}$. Region IV reaches equilibrium in 0.6 ns, as shown in Fig. 2(b-iv).

The water molecules are forced to break their hydrogen bonds by external pressure upon entering the (7, 7) CNT arm. It takes ≈ 0.22 eV of energy to break a hydrogen bond [57,58]. In the (7, 7) CNT, the reduction of the total number of hydrogen bonds directly results in a local energy loss and forces a deceleration of the imbibition process. In the (7, 7) CNT arm, the energy change results in a change in the imbibition rate at the two junctions. After 1.4 ns, it can be observed that the MCCNTs are filled, and from this point on, the average speed (v_z) of the water molecules in each zone becomes almost constant (Fig. 2d).

Next, we examine how MCCNTs filled with water compare to pristine CNTs filled with water. Fig. 4 shows the imbibition length in each nanochannel at a pressure difference equal to 250 MPa. The imbibition length is the waterfront distance between the inlet of a nanochannel and where the meniscus forms [39,59,40,41]. Using the positions of the atoms every 10 ps, we calculate the imbibition length. The calculation involves measuring the distance of the front row of oxygen atoms from the inlet of the nanochannel, which corresponds to the static graphene sheet inlet. It describes the type of imbibition observed by the temporal evolution of the imbibition length. The so-called filling rate of the imbibition is defined as the derivative of its temporal profile. The temporal evolution of the imbibition length describes the type of observed imbi-

bition. Generally, filling rates are calculated as derivatives of temporal profiles of imbibition lengths. The Lucas-Washburn formula describes the imbibition length for spontaneous capillary flow in parallel cylindrical tubes [60]; since it was first introduced, it has been extended to describe imbibition in porous materials and in nanopores [61].

The imbibition length evolution curve of the (14, 14) CNT up to approximately 0.17 ns is almost linear, corresponding to a constant filling rate (~ 50 m/s). After 0.6 ns, the (7, 7) CNT is filled with water, which is consistent with the fact that filling the (7, 7) CNT with water takes 3.2 times longer than filling the (14, 14) CNT, as listed in Table 1. The result for $\Delta p = 250$ MPa is a limiting case of the imbibition of the (7, 7) CNT; thus, the permeating water oscillates forward and backward. Oscillations are visible in the green curve of Fig. 4. In contrast, the imbibition profile (the red line in Fig. 4) of the MCCNT is neither a linear nor a squared-root-like function of time. The MCCNT has a topologically complex shape and shows a piece-wise linear imbibition profile. The imbibition filling rate is ~ 50 m/s in $0 \le t \le 0.06$ ns, which matches the filling behavior of the pristine (14, 14) CNT. On the other hand, for the time between $0.2 \le t \le 0.6$ ns, the filling rate is computed at ~ 8 m/s. At this interval, the filling rate in the (7, 7) CNT arm of the MCCNT matches the one in the pristine (7, 7) CNT. The imbibition length profile of MCCNTs oscillates more significantly as water molecules pass through the outlet Y-junction and fill the left (14, 14) CNTs. The filling of the outlet junction alone consumes 46% of the overall imbibition duration, making the outlet junction the most critical region during the imbibition of the MCCNT. $L(t) = 52.74t$ is the best fit for the imbibition length curve of the (14, 14) CNT, whereas $L(t) = 8.105t^{1/2}$ is the best fit for the profile of the (7, 7) CNT. In Fig. 4, the dashed lines indicate the two curve fits. Our MD simulation results, therefore, reveal that the (14, 14) CNT has a linear imbibition profile, which agrees with the results of previous studies for nanotube permeation [24]. In contrast, the imbibition of the (7, 7) CNT follows a square-root relation with time.

What makes the (14, 14) CNT different from the (7, 7) CNT for water imbibition? The original Lucas-Washburn formula describes a spontaneous capillary phenomenon of water in a hydrophilic cylindrical channel under a no-slip condition. However, considering the general case, it is necessary to create a formula that includes even a slip boundary condition at the wall. CNTs and Graphene without defects are excellent lubricants at nano- and microscales. Therefore, it is highly likely that water molecules entering the CNT slide off the tube wall. Since this violates the assumption that there is no slippage, the original Lucas-Washburn formula is incompatible with the imbibition length profile of the water inside the CNT. According to a recent study, various properties of water nanostructures within CNTs depend on their lengths and radii. The Lucas-Washburn formula has been corrected to take this into account [61]. The modified Lucas-Washburn formula consists of two terms that describe nanoscale effects, specifically radius-dependent slippage effects and length- and radius-dependent entrance effects, due to the variation of the orifice variation at the entrance. The term describing entrance effects has a linear dependency with time, whereas the term describing slip effects has a non-linear dependency with time. Because the number of water molecules inside a nanotube with a sub-nanometer diameter like the (7, 7) CNT is small, thermodynamic fluctuations are severe, and the number of hydrogen bonds per molecule is small. Consequently, the surface tension, slip length, and viscosity of the water nanochain are very different from those of bulk water. The temporal profile of the imbibition length of water inside the nanotube with a sub-nm diameter showcases a different behavior, because the entrance effects are negligible compared to the slip effects present.

3.2. Steady-state transport

Now, we turn to the steady-state transport of water through the MCCNT and compare it to the water flows through the pristine (7, 7) and (14, 14) CNTs. We are interested in how the MCCNT's complex geometry affects overall and local water transport. CNTs are connected to two filled water reservoirs. The water volume in each CNT corresponds to the final instance of the filling process in Section 3.1. For all simulations, we apply a pressure of 500 MPa on the outer graphene sheet of one of the water reservoirs.

In this study, we compute the accumulating volume of water in the outlet reservoir and the flow rates through the MCCNT and pristine (7, 7) and (14, 14) CNTs with equal lengths. We average the results over five simulation samples. In Fig. S3 of SI, additional information about the calculation of flow rates through nanotubes is provided. The flow rate Q is the volume of fluid passing through an area during a given period, which can be written as follows:

$$Q = \frac{\Delta V}{\Delta t},$$

where ΔV is the local volume and Δt is the elapsed time. The MCCNT has two (7, 7) CNT arms, and its cross-sectional area at its narrowest point is approximately double that of a (7, 7) CNT. According to the Hagen-Poiseuille equation, the ratio of volumetric flow rates with the same pressure difference (Δp) and the length of the tube is inversely proportional to the square of their cross-sectional area. On the other hand, the ratio of the volumetric flow rates, Q_{HP}, in the pristine (14, 14) and (7, 7) CNTs is 16 for the same applied pressure difference (Δp), the same length of the CNTs (L) and respective radii, $R_{(14,14)} = 2R_{(7,7)}$. The value deviates slightly from the ratio computed from simulations, $\frac{Q_{(14,14)}}{Q_{(7,7)}} \approx 16.5$.

Additionally, we examine the dynamics of steady-state water transport through the MCCNT to determine the effect of the Y-junctions on local water transport. We consider five zones of interest in the axial direction of the MCCNT, corresponding to the inlet and outlet (14, 14) CNT regions, the inlet and outlet Y-junction regions, and the (7, 7) CNT region, as shown in Fig. 2a. The steady-state axial velocity v_z, number of water molecules N_{H_2O}, and pair potential energy between water and carbon $V_{p,C-O}$ per water molecule are calculated directly from the MD simulations with a frequency of 100 simulation steps (= 0.1 ps) in each axial zone (see SI, Fig. S4). The local mass flow rate is defined as

$$\rho Q = \rho A_\perp v_{z,ave},$$

where $A_\perp$ is the local cross-sectional area and ρ is the local density. The local density, ρ is calculated as

$$\rho = \frac{N_{H_2O}\, m_{H_2O}}{A_\perp d_z},$$

where d_z is the length of each zone in the axial direction of the nanochannel (= 12 Å). N_{H_2O} and m_{H_2O} are the number of H_2O molecules and mass of a H_2O molecule, respectively. Therefore, the computation of the local flow rate is simplified to

$$\rho Q = \frac{N_{H_2O}\, m_{H_2O}\, v_{z,ave}}{d_z}.$$

The statistical values are obtained from five simulation samples, with different initial velocity distributions specified for each simulation.

We compare the local averages of axial velocity v_z, the number of water molecules N_{H_2O}, and the flow rate in the MCCNT with the corresponding local averages from the pristine (14, 14) and (7, 7) CNTs. For all nanotubes investigated, the flow rate ρQ remains nearly uniform at every local position in the steady-state channel. It matches the average values calculated from the accumulating mass in the outlet water reservoir (Table 2). However, the local density and the local axial velocity in the MCCNT prove to be non-uniform and asymmetrical, which is related to the non-uniform interaction energy $V_{p,C-O}$ between the carbon atoms in the nanotube and the oxygen atoms in the water molecules in the five regions of the MCCNT. As the interaction energy is reduced, the water molecule's local axial velocity v_z becomes faster. At Δp = 500 MP, the (14, 14) CNT region contains four times as many water molecules with four times the cross-sectional area as a (7, 7) CNT arm

Table 2
The steady-state process of water transport through MCCNTs. The following observables are presented as statistical averages with standard deviations: velocity v_z, number of water molecules N_{H_2O}, local mass flow rate ρQ. The averages are computed locally for the five spatial regions of the MCCNT denoted in Fig. 2a and the pristine (14, 14) and (7, 7) CNTs. The statistical measures for the interaction energy between carbon and oxygen of the water molecule, $V_{p,C-O}$ solely in the MCCNT regions, are also reported. The statistical measures are calculated over a sample of 5 simulations, where observables were written for the last 2 ns of the total simulation time of 5 ns. The table columns represent the spatial regions along the tube axis reported in Fig. 2a. The rows of the table represent the observables. The table is split into three sections, each for every nanotube studied [MCCNT, (14, 14) CNT, and (7, 7) CNT]. Graphs for all observables for the different nanotubes are summarized in Fig. S4 in the SI.

Region	I	II	III	IV	V
	MCCNT				
v_z (m/s)	4.78 ± 0.04	11.55 ± 0.07	21.33 ± 0.43	16.0 ± 0.24	6.43 ± 0.53
N_{H_2O}	76 ± 0.15	32 ± 0.1	17 ± 0.1	23 ± 0.6	58 ± 4.3
ρ Q (1000 $\frac{kg}{m^3}\frac{\mu m^3}{s}$)	9.13 ± 0.001	9.14 ± 0.001	9.1 ± 0.001	9.35 ± 0.003	9.34 ± 0.06
$V_{p,C-O}$ (kcal/mol)	66.6 ± 0.14	53.1 ± 0.06	36.6 ± 0.3	40.3 ± 0.8	48.3 ± 3.9
	(14, 14) CNT				
v_z (m/s)	20.0 ± 0.1	20.1 ± 0.1	20.1 ± 0.1	20.1 ± 0.1	20.1 ± 0.1
N_{H_2O}	78 ± 0.1	78 ± 0.1	78 ± 0.05	77 ± 0.1	77.5 ± 0.1
ρ Q (1000 $\frac{kg}{m^3}\frac{\mu m^3}{s}$)	39.0 ± 0.002	39.0 ± 0.002	39.0 ± 0.002	39.0 ± 0.003	39.0 ± 0.002
	(7, 7) CNT				
v_z (m/s)	9.5 ± 0.3	9.9 ± 0.4	9.9 ± 0.4	9.8 ± 0.2	10.1 ± 0.4
N_{H_2O}	9.9 ± 0.2	9.6 ± 0.3	9.4 ± 0.4	9.3 ± 0.3	9.2 ± 0.4
ρ Q (1000 $\frac{kg}{m^3}\frac{\mu m^3}{s}$)	2.34 ± 0.002	2.38 ± 0.003	2.34 ± 0.004	2.3 ± 0.004	2.31 ± 0.003

(Table 2, region III *vs.* I). The axial velocity has the opposite trend, indicating acceleration and deceleration of the flow near the inlet and outlet Y-junctions of the MCCNT. Additionally, v_z in region IV is ≈ 1.4 times larger than in region II, as listed in Table 2. The volumetric flow rate is almost constant in pristine (14, 14) CNTs. As a result of its narrow inside, the water inside the pure (7, 7) CNT is difficult to model as a continuous fluid. So the flow rate has some variation. We find that the flow rate changes by about 4% in region I. In this water nanostructure, the number of hydrogen bonds per molecule is small, making it inappropriate to consider it as a continuum.

This phenomenon also occurs in the MCCNT. At each position along the MCCNT axis, the water density is not uniform but depends on the local cross-sectional area. We calculate the spatial profiles of the cross-sectional area $A_\perp$, the local density ρ, the local velocity v_z, and the mass flow rate $\dot{m} = \rho A_\perp v_z$ in the axial direction of the MCCNT structure to assess how the cross-sectional area affects flow characteristics along the MCCNT axis. In steady-state simulations, atomic positions are dumped every 0.1 ps for the last 2 ns. Using a simple finite difference scheme, we determine the velocities of water molecules in the MCCNT. As the length of the MCCNT is divided into 1-nm bins, the local average velocity v_z (Fig. 5b, solid line) and the number of water molecules N_{H_2O} in each bin are calculated. A total of five simulation samples are averaged, each with a different distribution of initial velocity. Moreover, the local cross-sectional area of the MCCNT varies. An elliptical cross-section forms when a wide (14, 14) CNT is bifurcated into two narrower (7, 7) CNT arms. The effective elliptical cross-sectional area distribution along axial direction z is calculated from MCCNT's coordinate file (see Fig. 5a). O and H atoms in H_2O have equilibrium distances from the tube surface of 3.3 and 2.2 Å, respectively, when they are confined inside CNTs. Therefore, in calculating the effective cross-sectional area of the nanochannel, we exclude the regions within 2.2 Å of the CNT surface. As a dotted line, the water density distribution along the MCCNT axis ρ is shown in Fig. 5a. Along the MCCNT axis, the local mass flow rate, $\dot{m} = \rho A_\perp v_z$ remains constant (see Fig. 5b).

Fig. 5 shows the local profiles of water density (ρ), cross-sectional area ($A_\perp$), velocity (v_z), and mass flow rate ($\dot{m}$) along the tube axis. The inlet Y-junction acts as the main congestion region in the MCCNT structure, as water density reaches a maximum right before the Y-junction region and a minimum at the end of the Y-junction region. It is not so that water molecules slow down in congestion but rather that the distance between them decreases due to the increased local density.

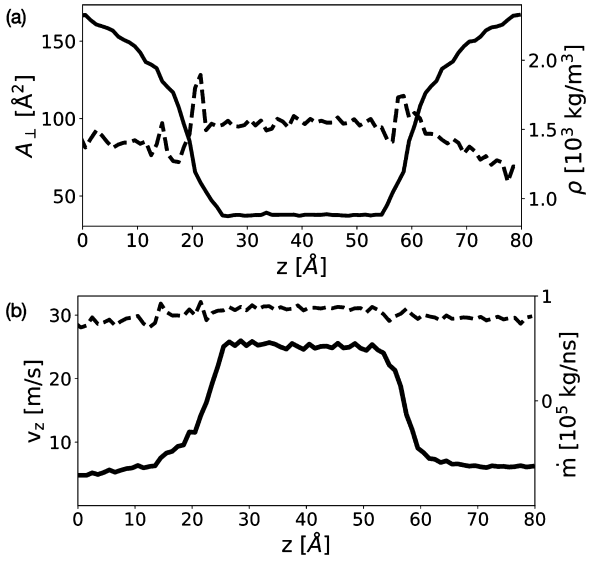

Fig. 5. (a) The cross-sectional area $A_\perp$ distribution (solid line) and the steady-state density ρ distribution (dotted line) along the length of the MCCNT. (b) The distributions of the steady-state axial velocity v_z (solid line) and of the steady-state mass flow rate $\dot{m}$ (dotted line) along the length of the MCCNT. All "steady-state" variables are averaged over the last 2 ns of simulation time.

The inlet (14, 14) CNT and inlet Y-junction regions have a greater concentration of water molecules than the outlet (14, 14) CNT and outlet Y-junction regions. Besides, the water velocity v_z in the MCCNT significantly increases in the inlet junction region compared to the outlet junction. This difference in the slope of the velocity profile between the two junction regions is related to a 32% increase in the local average of potential energy $V_{p,C-O}$ in the inlet junction region, compared to the outlet junction region (for the comparison, see SI, Fig. S4 and Table 2). At the inlet junction, water flow is staggered, resulting in local water compression. Compressed water is rapidly released into the (7, 7) arm of the MCCNT. Interestingly, the number of neighboring water molecules of each H_2O molecule decreases in the vicinity of the junction, where the (14, 14) CNT arms are deformed, and the cross-sectional area decreases. The reduction of neighboring water molecules translates to a local decrease in the number of hydrogen bonds, resulting in energy loss and causing velocity changes at the junctions.

4. Conclusions

We performed classical MD simulations to study the nonequilibrium water filling and steady-state water transport through an MCCNT structure connected to two water reservoirs. A significant factor in the filling process of the MCCNT is whether the water flow overcomes the outlet junction region (Fig. 4), which consumes 46% of the time filling the MCCNT end-to-end. Interestingly, we find that the MCCNT imbibes more efficiently than the pristine (7, 7) CNT of the same length, with a decreased imbibition time of 15%. We show that the complex geometry's imbibition profile changes between the (14, 14) and (7, 7) CNTs within the Y-junctions. The flow characteristics at the Y-junctions constrain the steady-state water transport through the MCCNT. Macroscopic fluid mechanics may describe the transport characteristics in the CNT regions for steady-state transport. However, Y-junctions are characterized by atomic-scale phenomena depending on whether the flow is split from the (14, 14) to the (7, 7) CNT or merged from the (7, 7) to the (14, 14) CNT. We identify the inlet junction as a spatial zone of particular interest in the MCCNT structure because the volume of water is congested in the region before the (7, 7) CNT arm. As the number of hydrogen bonds in the water molecules in the (7, 7) CNTs decreases, the system's energy decreases locally, causing congestion of the flow at the junction region. The scope of this computational study on water nanoflow in CNTs with complex morphology is to support the design of future nanochannels that can adapt to complex geometries for applications such as water purification and desalination, and drug delivery.

Declaration of competing interest

The authors declare that they have no known competing financial interests or personal relationships that could have appeared to influence the work reported in this paper.

Acknowledgements

This work is supported by the European Research Council Advanced Investigator Award (Grant No. 341117) and the National Research Foundation (NRF) of Korea grant funded by the Korean government (Grant No. NRF-2016R1A2B2016120; NRF-2020R1A6A1A03043435). We acknowledge the Swiss National Supercomputing Centre (CSCS) for computing time through project s930. We would like to acknowledge Prof. Jens H. Walther for his fruitful comments.

Appendix A. Supplementary material

Supplementary material related to this article can be found online at https://doi.org/10.1016/j.cap.2022.11.003.

References

[1] P.J.J. Alvarez, C.K. Chan, M. Elimelech, N.J. Halas, D. Villagrán, Emerging opportunities for nanotechnology to enhance water security, Nat. Nanotechnol. 13 (2018) 634–641.
[2] M.F.L.D. Volder, S.H. Tawfick, R.H. Baughman, A.J. Hart, Carbon nanotubes: present and future commercial applications, Science 339 (2013) 535–540.
[3] M. Majumder, N. Chopra, R. Andrews, B.J. Hinds, Enhanced flow in carbon nanotubes, Nature 438 (2005) 43–44.
[4] J.K. Holt, H.G. Park, Y. Wang, M. Stadermann, A.B. Artyukhin, C.P. Grigoropoulos, A. Noy, O. Bakajin, Fast mass transport through sub-2-nanometer carbon nanotubes, Science 312 (2006) 1034–1037.
[5] J.A. Thomas, A.J.H. McGaughey, O. Kuter-Arnebeck, Pressure-driven water flow through carbon nanotubes: insights from molecular dynamics simulation, Int. J. Therm. Sci. 49 (2010) 281–289.
[6] J.H. Walther, K. Ritos, E.R. Cruz-Chu, C.M. Megaridis, P. Koumoutsakos, Barriers to superfast water transport in carbon nanotube membranes, Nano Lett. 117 (2017) 1910–1914.
[7] L. Liu, G.N. Patey, A molecular dynamics investigation of the influence of water structure on ion conduction through a carbon nanotube, J. Chem. Phys. 146 (2017) 074502.
[8] Y. Zhang, Transport in nanotube tree, Int. J. Heat Mass Transf. 114 (2017) 536–540.
[9] W.Z. Li, J.G. Wen, Z.F. Ren, Straight carbon nanotube Y-junctions, Appl. Phys. Lett. 79 (2001) 1879–1881.
[10] M. Zhang, J. Li, Carbon nanotube in different shapes, Mater. Today 12 (2009) 12–18.
[11] E. Secchi, S. Marbach, A. Nigues, D. Stein, A. Siria, L. Bocquet, Massive radius-dependent flow slippage in carbon nanotubes, Nature 537 (2016) 210–213.
[12] T. Werder, J.H. Walther, R.L. Jaffe, T. Halicioglu, P. Koumoutsakos, On the water-carbon interaction for use in molecular dynamics simulations of graphite and carbon nanotubes, J. Phys. Chem. B 107 (2003) 1345–1352.
[13] S. Joseph, N. Aluru, Why are carbon nanotubes fast transporters of water?, Nano Lett. 8 (2008) 452–458.
[14] J. Thomas, A.J.H. Mcgaughey, Reassessing fast water transport through carbon nanotubes, Nano Lett. 8 (2008) 2788–2793.
[15] J.A. Thomas, A.H. McGaughey, Water flow in carbon nanotubes: transition to subcontinuum transport, Phys. Rev. Lett. 102 (2009) 1.
[16] E. Brini, C.J. Fennel, M. Fernandez-Serra, B. Hribar-Lee, M. Lukšič, K.A. Dill, How water's properties are encoded in its molecular structure and energies, Chem. Rev. 13 (2013) 12385–12414.
[17] F. Shayeganfar, J. Beheshtian, R. Shahsavari, First-principles study of water nanotubes captured inside carbon/boron nitride nanotubes, Langmuir 34 (2018) 11176–11187.
[18] A.G. Donchev, N.G. Galkin, A.A. Illarionov, O.V. Khoruzhii, M.A. Olevanov, V.D. Ozrin, M.V. Subbotin, V.I. Tarasov, Water properties from first principles: simulations by a general-purpose quantum mechanical polarizable force field, Proc. Natl. Acad. Sci. USA 103 (2006) 8613–8617.
[19] C. Wongchoosuk, S. Krongsuk, T. Kerdcharoen, First principles and md simulation study of the interaction of functionalized carbon nanotubes with water molecules, in: IEEE NANO, vol. 7, 2007, pp. 1130–1134.
[20] L. Wang, J. Zhao, F. Li, H. Fang, J. Lu, First-principles study of water chains encapsulated in single-walled carbon nanotube, J. Phys. Chem. C 113 (2009) 5368–5375.
[21] M.C.G. Lim, Z.W. Zhong, The junction size effect on the electromigration flow of copper atoms through carbon-nanotube junctions, Physica E, Low-Dimens. Syst. Nanostruct. 43 (2011) 862–868.
[22] P. Robert, Physical Properties of Carbon Nanotube/Graphene Junctions, Ph.D. thesis, Karlsruhe Institute for Technology, 2010.
[23] I. Hanasaki, A. Nakatani, Water flow through carbon nanotube junctions as molecular convergent nozzles, Nanotechnology 17 (2006) 2794–2804.
[24] F. Ebrahimi, F. Ramazani, M. Sahimi, Nanojunction effects on water flow in carbon nanotubes, Sci. Rep. 8 (2018) 075505.
[25] K. Sattler, Handbook of Nanophysics: Nanotubes and Nanowires, CRC Press, 2018.
[26] H. Wu, J. Qiu, C. Hao, Y. Li, Simulation study of hydrogen storage in two kinds of y-junction carbon nanotubes, in: IEEE-NANO, vol. 2, 2003, pp. 678–681.
[27] A. Cummings, M. Osman, D. Srivastava, M. Menon, Thermal conductivity of Y-junction carbon nanotubes, Phys. Rev. B 70 (2004) 3.
[28] X. Li, S. Wang, Flow field and pressure loss analysis of junction and its structure optimization of aircraft hydraulic pipe system, Chin. J. Aeronaut. 26 (2013) 1080–1092.
[29] B.C. Satishkumar, P.J. Thomas, A. Govindaraj, C.N.R. Rao, Y-junction carbon nanotubes, Appl. Phys. Lett. 77 (2000) 2530–2532.
[30] J.M. Romo-Herrera, M. Terrones, H. Terrones, S. Dag, V. Meunier, Covalent 2d and 3d networks from 1d nanostructures: designing new materials, Nano Lett. 7 (2007) 570–576.
[31] L.P. Rajukumar, M. Belmonte, J.E. Slimak, A.L. Elías, E. Cruz-Silva, N. Perea-López, A. Morelos-Gómez, H. Terrones, M. Endo, P. Miranzo, M. Terrones, Covalent networks: 3d nanocomposites of covalently interconnected multiwalled carbon nanotubes with sic with enhanced thermal and electrical properties, Adv. Funct. Mater. 25 (2015) 4985–4993.
[32] P.J.F. Harris, I. Suarez-Martinez, N.A. Marks, The structure of junctions between carbon nanotubes and graphene shells, Nanoscale 8 (2016) 18849–18854.
[33] M. Terrones, F. Banhart, N. Grobert, J.C. Charlier, H. Terrones, P.M. Ajayan, Molecular junctions by joining single-walled carbon nanotubes, Phys. Rev. Lett. 89 (2002) 1.
[34] M. Yoon, S. Han, G. Kim, S.B. Lee, S. Berber, E. Osawa, J. Ihm, M. Terrones, F. Banhart, J.C. Charlier, N. Grobert, H. Terrones, P.M. Ajayan, D. Tománek, Zipper mechanism of nanotube fusion: theory and experiment, Phys. Rev. Lett. 92 (2004) 5.
[35] Y. Zhen, H.W.C. Postma, L. Balents, C. Dekker, Carbon nanotube intramolecular junctions, Nature 402 (1999) 273–276.
[36] V.I. Tsebro, O.E. Omel'yanovskii, Undamped currents and magnetic field trapping in a multi-connected, carbon nanotube structure, Phys. Usp. 170 (2000) 847–853.
[37] L.P. Biró, Z.E. Horváth, G.I. Márk, Z. Osváth, A.A. Koós, A.M. Benito, W. Maser, P. Lambin, Carbon nanotube Y-junctions: growth and properties, Diam. Relat. Mater. 13 (2004) 241–249.
[38] T. Kim, G.W. Kim, H. Jeong, G. Kim, S. Jang, Equilibrium structures of water molecules confined within a multiply connected carbon nanotube: a molecular dynamics study, Phys. Chem. Chem. Phys. 20 (2020) 252–257.
[39] E. Oyarzua, J.H. Walther, A. Mejia, H.A. Zambrano, Early regimes of water capillary flow in slit silica nanochannels, Phys. Chem. Chem. Phys. 17 (2015) 14731–14739.
[40] A. Budaraju, J. Phirani, S. Kondaraju, S.S. Bahga, Capillary displacement of viscous liquids in geometries with axial variations, Langmuir 32 (2016) 10513–10521.
[41] B. Zhmud, F. Tiberg, K. Hallstensson, Dynamics of capillary rise, J. Colloid Interface Sci. 228 (2000) 263–269.

[42] Q. Chen, Q. Wang, Y. Liu, T. Wu, The effect of hydrogen bonds on diffusion mechanism of water inside single-walled carbon nanotubes, J. Chem. Phys. 140 (2014) 214507.
[43] M.E. Tuckerman, J. Alejandre, R. Lòpez-Rendón, A.L. Jochim, G.J. Martyna, A Liouville-operator derived measure-preserving integrator for molecular dynamics simulations in the isothermal–isobaric ensemble, J. Phys. A, Math. Gen. 39 (2006) 5629–5651.
[44] D. Frenkel, B. Smit, Understanding Molecular Simulation, Academic Press, 2002.
[45] M.E. Suk, N.R. Aluru, Modeling water flow through carbon nanotube membranes with entrance / exit effects, Nanoscale Microscale Thermophys. Eng. 21 (2017) 247–262.
[46] S. Plimpton, Fast parallel algorithms for short-range molecular dynamics, J. Comput. Phys. 117 (1995) 1–19.
[47] V. Kräutler, W.F. Van Gunsteren, P.H. Hünenberger, A fast SHAKE algorithm to solve distance constraint equations for small molecules in molecular dynamics simulations, J. Comput. Chem. 22 (2001) 501–508.
[48] H.W. Horn, W.C. Swope, J.W. Pitera, J.D. Madura, T.J. Dick, G.L. Hura, T. Head-Gordon, Development of an improved four-site water model for biomolecular simulations: TIP4P-Ew, J. Chem. Phys. 120 (2004) 9665–9678.
[49] J. Alejandre, G.A. Chapela, The surface tension of TIP4P/2005 water model using the Ewald sums for the dispersion interactions, J. Chem. Phys. 132 (2010) 014701.
[50] W.L. Jorgensen, J. Chandrasekhar, J.D. Madura, R.W. Impey, M.L. Klein, Comparison of simple potential functions for simulating liquid water, J. Chem. Phys. 79 (1983) 926–935.
[51] M. Deserno, C. Holm, How to mesh up Ewald sums. I. A theoretical and numerical comparison of various particle mesh routines, J. Chem. Phys. 109 (1998) 7678–7693.
[52] S.L. Mayo, B.D. Olafson, W.A. Goddard, DREIDING: a generic force field for molecular simulations, J. Phys. Chem. 94 (1990) 8897–8909.
[53] T. Werder, J.H. Walther, R.L. Jaffe, T. Halicioglu, F. Noca, P. Koumoutsakos, Molecular dynamics simulation of contact angles of water droplets in carbon nanotubes, Nano Lett. 1 (2001) 697–702.
[54] F. Taherian, V. Marcon, N.F.A. van der Vegt, F. Leroy, What is the contact angle of water on graphene?, Langmuir 29 (2013) 1457–1465.
[55] W. Humphrey, A. Dalke, K. Schulten, VMD – visual molecular dynamics, J. Mol. Graph. 14 (1996) 33–38.
[56] WCCNT, https://github.com/cselab/wccnt. (Accessed 13 July 2019).
[57] X. Xu, W.A. Goddard III, Bonding properties of the water dimer: a comparative study of density functional theories, J. Phys. Chem. A 108 (2004) 2305–2313.
[58] V.S. Bryantsev, M.S. Diallo, A.C.T. van Duin, W.A. Goddard III, Evaluation of B3LYP, X3LYP, and M06-class density functionals for predicting the binding energies of neutral, protonated, and deprotonated water clusters, J. Chem. Theory Comput. 5 (2009) 1016–1026.
[59] J. Kim, H. Kim, On the dynamics of capillary imbibition, J. Mech. Sci. Technol. 26 (2012) 3795–3801.
[60] V.M. Starov, M.G. Velarde, C.J. Radke, Wetting and Spreading Dynamics, CRS Press, 2007.
[61] M. Heiranian, N.R. Aluru, Modified Lucas-Washburn theory for fluid filling in nanotubes, Phys. Rev. E 105 (2022) 055105.